

# Faraday Discussions

Accepted Manuscript



This manuscript will be presented and discussed at a forthcoming Faraday Discussion meeting. All delegates can contribute to the discussion which will be included in the final volume.

**Register now to attend!** Full details of all upcoming meetings: <http://rsc.li/fd-upcoming-meetings>



This is an *Accepted Manuscript*, which has been through the Royal Society of Chemistry peer review process and has been accepted for publication.

*Accepted Manuscripts* are published online shortly after acceptance, before technical editing, formatting and proof reading. Using this free service, authors can make their results available to the community, in citable form, before we publish the edited article. We will replace this *Accepted Manuscript* with the edited and formatted *Advance Article* as soon as it is available.

You can find more information about *Accepted Manuscripts* in the [Information for Authors](#).

Please note that technical editing may introduce minor changes to the text and/or graphics, which may alter content. The journal's standard [Terms & Conditions](#) and the [Ethical guidelines](#) still apply. In no event shall the Royal Society of Chemistry be held responsible for any errors or omissions in this *Accepted Manuscript* or any consequences arising from the use of any information it contains.



## Faraday Discussions

## Paper

## Sn<sub>x</sub>Ti<sub>1-x</sub>O<sub>2</sub> Solid-solution-nanoparticle Embedded Mesoporous Silica (SBA-15) Hybrid as an Engineered Photocatalyst with Enhanced Activity

Received 00th January 20xx,  
Accepted 00th January 20xx

DOI: 10.1039/x0xx00000x

www.rsc.org/

N. R. Srinivasan,<sup>a</sup> Rajdip Bandyopadhyaya\*<sup>a</sup>

Synthesis of hybrids of a porous host-material (with well-dispersed embedded nanoparticles inside the pore), wherein each nanoparticle have precisely controlled properties (size and composition) poses a generic challenge. To this end, a new strategy is proposed to form Sn<sub>x</sub>Ti<sub>1-x</sub>O<sub>2</sub> solid-solution-nanoparticles inside the pores of sphere-like mesoporous silica (SBA-15), with different percentages of Sn in the nanoparticle (varying from 5 to 50 at.%), for enhanced photocatalysis. X-ray diffraction confirms the formation of solid-solution nanoparticles in the porous silica hybrid, while the location of nanoparticles and elemental composition are identified using electron microscopy. The hybrid with 5 at.% of Sn (Sn<sub>0.05</sub>Ti<sub>0.95</sub>O<sub>2</sub>-sphere-like SBA-15) shows the maximum photocatalytic activity for degradation of rhodamine-B dye (first order rate constant for degradation,  $k=1.86\text{ h}^{-1}$ ), compared to both pure TiO<sub>2</sub>-sphere-like SBA-15 ( $k=1.38\text{ h}^{-1}$ ) or pure SnO<sub>2</sub>-sphere-like SBA-15 ( $k=0.14\text{ h}^{-1}$ ) or other hybrids in this series. XPS and PL spectra suggest the formation of more oxygen vacancies during the replacement of Ti<sup>4+</sup> with Sn<sup>4+</sup>. Electrochemical studies reveal that there is a reduction of charge transfer resistance from 910 KΩ cm<sup>-2</sup> for TiO<sub>2</sub>-sphere-like SBA-15, to 332 KΩ cm<sup>-2</sup> for Sn<sub>0.05</sub>Ti<sub>0.95</sub>O<sub>2</sub>-sphere-like SBA-15. These results imply that the enhancement in photocatalytic performance is as a result of delay in recombination of charge carries. Therefore, the approach followed in the present work to form solid-solution nanoparticles inside a porous host without causing pore blockage, would be a promising route towards increasing reaction rates in catalytic applications of hybrid materials.

### Introduction

Semiconductor mediated photocatalysts have been extensively investigated to degrade organic pollutants such as toxic dyes, pesticides, pharmaceutical compounds etc., present in wastewater.<sup>1-4</sup> This technique is a suitable alternative to treat wastewater without releasing harmful products, as other technologies like adsorption by activated carbon, solvent extraction, ozonation etc. produce secondary pollutants that are hazardous.<sup>5,6</sup> Photocatalysis over a semiconductor particle surface is initiated by absorption of photon having energy equal to or greater than the semiconductor band gap, thereby producing charge carriers such as electrons and holes.<sup>7</sup> Once these charge carriers reach the semiconductor surface, they undergo a series of reactions with adsorbed molecules to degrade the latter completely.<sup>8</sup>

Among semiconductor photocatalysts, TiO<sub>2</sub> is the most promising due to its high photocatalytic efficiency, non-toxicity, and low cost.<sup>9,10</sup> However, the major drawback of TiO<sub>2</sub> is the very fast recombination of its charge carriers (~10 -100 ns). As a result, only a fraction of them are

responsible for reaction with the adsorbed molecules (~100 ns - 10 ms). The remaining charge carriers recombine and release energy in the form of heat or luminescence.<sup>8</sup> Hence, this leads to a significant reduction in photocatalytic efficiency. Thus, TiO<sub>2</sub> is not suitable for industrial applications because of recombination of charge carriers, interparticle aggregation, and reusability issues.

Over the past few years, coupled semiconductor photocatalysts have been in focus, primarily to exploit the synergetic effect arising from the presence of two different electronic structures of two semiconductor materials, compared to only one semiconductor material. To achieve this, the following strategies such as, deposition of noble metals (e.g., Ag, Au, Pt, Pd, etc.) on the semiconductor particle;<sup>11-13</sup> doping by metal ion (Fe, Cr, Mn, V, etc.);<sup>14-16</sup> or by non-metal doping (C, N, S, B, F etc.) into semiconductor;<sup>1,17-20</sup> and coupled semiconductors (SnO<sub>2</sub>/TiO<sub>2</sub>, CdS/TiO<sub>2</sub>, Bi<sub>2</sub>S<sub>3</sub>/Bi<sub>2</sub>WO<sub>6</sub> etc.)<sup>21-23</sup> have been explored so far. For example, coupling of SnO<sub>2</sub> (band gap of bulk SnO<sub>2</sub> ~ 3.8eV) with another semiconductor TiO<sub>2</sub> (band gap of bulk TiO<sub>2</sub> ~ 3.2eV), shows an enhancement in photocatalytic activity, because of a good match in the energy levels of conduction and valence bands (ECB for SnO<sub>2</sub> = 0 V, vs. NHE at pH 7; ECB for TiO<sub>2</sub> = - 0.5 V vs. NHE at pH 7).<sup>23</sup> More importantly, photoexcited electrons shuttle from the conduction band of TiO<sub>2</sub> to the conduction band of SnO<sub>2</sub> due to this potential difference, whereas photoexcited holes

<sup>a</sup> Department of Chemical Engineering, Indian Institute of Technology Bombay, Powai, Mumbai 400076, India. Tel: +91 (22) 2576 7209; Fax: +91 (22) 2572 6895  
E-mail: rajdip@che.iitb.ac.in

† Electronic Supplementary Information (ESI) available: [XPS and PL Spectra]. See DOI: 10.1039/x0xx00000x

shuttle from the valence band of  $\text{SnO}_2$  to the valence band of  $\text{TiO}_2$ . This shuttling effect increases the charge separation, and thereby decreases the recombination of charge carriers.<sup>10</sup>

Coupled semiconductor photocatalyst is mostly made either in the form of individual core shell nanoparticles or thin films containing such core-shell nanoparticles to increase their accessibility against diffusing molecules.<sup>24-26</sup> In this regard, thin film will increase reusability of the photocatalyst, but results in low photocatalytic activity, because of its lower specific surface area than individual nanoparticles.<sup>26</sup> Similarly, the main challenge in the core-shell structure lies in achieving a uniform layer of shell-coating on the core nanoparticle, and also prevention of particle aggregation. Hence, coupled semiconductor nanoparticles in the form of a solid-solution does not have the issue of an uniform shell-coating, as the two metal ions are dispersed in the same lattice structure.<sup>27-31</sup> Moreover, it also provides the possibility of fine tuning of the band gap energy, by altering composition of the two metal components in the solid-solution. Therefore, it is necessary to focus on pathways to form nanostructured solid-solution photocatalysts.

The other challenge in prevention of interparticle aggregation can be addressed through embedding of the solid-solution nanoparticulate photocatalyst in porous hosts (zeolite, mesoporous silica etc.).<sup>32-37</sup> Among these hosts, mesoporous silica (SBA-15) has an uniform, but tunable, mesopore diameter (5-10 nm), high specific surface area (800-1000  $\text{m}^2\text{g}^{-1}$ ) and high specific pore volume (0.8-1.2  $\text{cm}^3\text{g}^{-1}$ ),<sup>38</sup> which are ideal features of a catalyst-host. These impart following advantages to SBA-15 as a host, if used for photocatalysis: (i) presence of mesopores of large diameter in the SBA-15 particle provides easy passage for efficient transport of reactants and products during photocatalytic reactions, (ii) hydrophilic nature of SBA-15 ensures that waste water with contaminants (like dye) in it can access the surface of the embedded photocatalyst without much diffusional resistance. (iii) stability of silica against reactive oxygen species during UV light irradiation. In many reports on semiconductor particle ( $\text{TiO}_2$ ,  $\text{SnO}_2$ ,  $\text{ZnO}$  etc.) embedded porous host (SBA-15)<sup>39</sup> as a photocatalyst, pores are either blocked by semiconductor particles or the latter grows on the external surface of SBA-15.<sup>40-44</sup> Therefore, embedding of nanostructured solid-solution photocatalyst within the porous host without pore blockage is still not achieved, which would translate into more photocatalytic sites, for a possible higher rate of dye degradation.

With this motivation, a new approach has been pursued to form  $\text{Sn}_x\text{Ti}_{1-x}\text{O}_2$  solid-solution-nanoparticle inside the mesopores of submicron sphere-like SBA-15 particles, without causing pore blockage. The influence of Sn content (5 to 50 at.%) in this hybrid has been demonstrated by relating the photocurrent response, with the photocatalytic activity towards degradation of rhodamine B under UV irradiation. The mechanism of photocatalytic activity has also been explained in detail for the first time, via their energy band diagram. The strategy used in this work would therefore provide a

methodology to prepare an assembly of solid solution nanoparticles in a porous, host-material for catalysis.

## Experimental

### Synthesis of $\text{Sn}_x\text{Ti}_{1-x}\text{O}_2$ -sphere-like SBA-15

The synthesis protocol for submicron sphere-like SBA-15 was according to our earlier work,<sup>33</sup> with inclusion of mesitylene in the reactant, for controlling the growth of SBA-15 particle. Typically, 3.6 g of P123 was added in a polypropylene beaker containing 140 ml of 2.5 M HCl solution and stirred at 35 °C until P123 was completely dissolved. Then, 7.74 g of TEOS was added drop wise with vigorous stirring (500 rpm) for 2 min and was kept under static condition at 35 °C. After 30 min, mesitylene (1.8 g) was added into the beaker containing silica particles (white precipitate), and stirred at 200 rpm for 2min. Then, the mixture was kept (without stirring) at 35 °C for 24 h, and subsequently transferred into a teflon coated closed vessel, which was kept at 100 °C for 24 h in an air oven. Thereafter, the resultant solid product was filtered, washed with water, and dried at 100 °C. Finally, the sample was calcined at 550 °C (temperature ramp of 1 °C/min) in presence of air for 4 h.

The protocol for embedding  $\text{SnO}_2$  nanoparticles inside the pores of SBA-15 was as follows. Typically, 100 mg of sphere-like SBA-15 particles were mixed with a solution containing 50  $\mu\text{l}$  of  $\text{SnCl}_4$  and 0.6 ml of isopropanol. Then, the mixture was put in a vial and kept under vacuum at 80 °C for 24 h to diffuse the Sn precursor inside the mesopores of sphere-like SBA-15. The samples were subsequently heated in presence of air at 550 °C for 6 h to obtain  $\text{SnO}_2$ -SBA-15. For the preparation of  $\text{TiO}_2$ -SBA-15, 100 mg of sphere-like SBA-15 particles were mixed with a solution containing 0.225 ml of TTIP and 0.5 ml of isopropanol. Afterwards, a similar procedure was followed, as above for the  $\text{SnO}_2$ -SBA-15 protocol. For  $\text{Sn}_x\text{Ti}_{1-x}\text{O}_2$  synthesis, different concentrations of  $\text{SnCl}_4$  and TTIP were mixed to vary  $x$  in the preparation of the solid-solution. Subsequently, similar steps were followed to form solid-solution-nanoparticles inside SBA-15 particles.

### Characterization techniques

Particle morphology and composition were analyzed using a FE-SEM (Model: JSM-7600F), attached with an EDX spectrometer, and also using a FEG-TEM (Model: JEM-2100F). XRD was done using a Philips X'Pert Pro diffractometer, with  $\text{CuK}\alpha$  radiation. Nitrogen and hydrogen sorption studies were performed using a Micromeritics ASAP 2020 system. UV-Vis diffuse reflectance spectra for all samples were recorded using a lamda 35 (Perkin-Elmer) spectrophotometer. X-ray photoelectron spectroscopy (XPS) experiments were carried out with a VG Scientific ESCALAB 220IXL instrument, using Al  $\text{K}\alpha$  X-ray radiation. Photoluminescence (PL) spectra were recorded using Perkin-Elmer LS 55 spectrofluorometer. Electrochemical impedance spectroscopy (EIS) was performed on a CHI660 electrochemical workstation (CH Instruments).

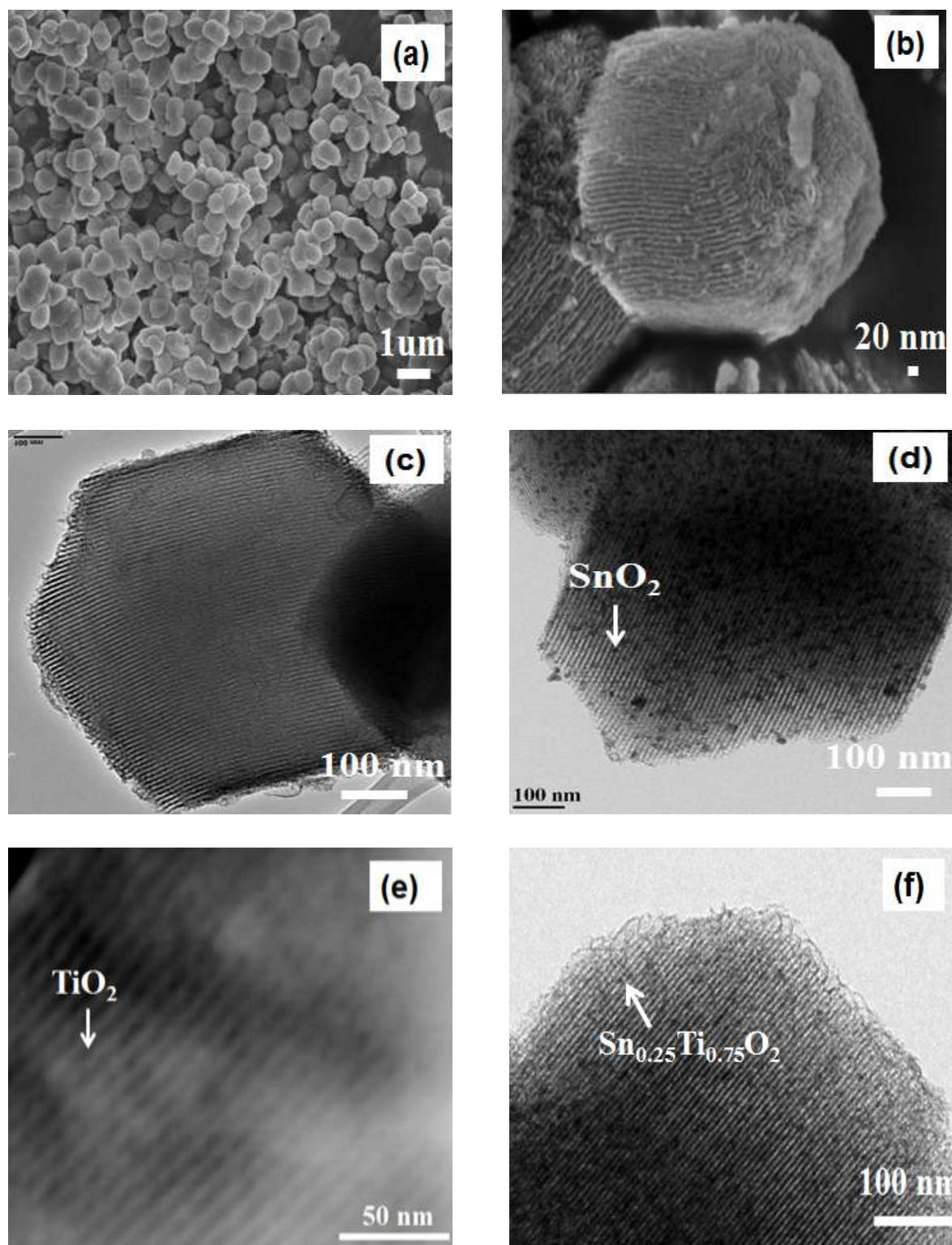


**Fig. 1** (a) and (b) SEM images of sphere-like SBA-15 (c) HRTEM image of sphere-like SBA-15 (d) HRTEM image of  $\text{SnO}_2$ -sphere like SBA-15 (e) HRTEM image of  $\text{TiO}_2$ - sphere-like SBA-15 (f) HRTEM image of  $\text{Sn}_{0.25}\text{Ti}_{0.75}\text{O}_2$ -sphere-like SBA-15.

#### Electrochemical analysis

10 mg of the photocatalyst and 20  $\mu\text{l}$  of nafion solution (5 wt.%) were dispersed in 2 ml ethanol (sonication for 2 min), after which, 100  $\mu\text{l}$  of the above dispersion was added onto FTO conductive glass and spin coated to form a working

electrode. Electrochemical studies were carried out under UV irradiation using a conventional three-electrode system made of quartz cell. Platinum foil and saturated calomel electrodes were used as counter and reference electrodes, respectively.

50 ml of 0.1 M KOH aqueous solution was degassed with nitrogen and used as an electrolyte.

### Photodegradation of rhodamine B dye

For photocatalytic degradation experiments, 100 mg of hybrid powder sample was taken in a quartz tube containing 100 ml of 50  $\mu$ M rhodamine B solution, kept under stirring. Above this dispersion, a 250 W high-pressure mercury lamp was placed, housed within a jacketed tube. Water was circulated through the annulus of the tube to avoid heating of the dispersion. After every 30 min, samples were withdrawn from the reactor, and centrifuged for 10 min at 15000 rpm, to avoid any scattering from suspended solids during absorbance measurement in the UV-Vis spectrophotometer. The concentration of rhodamine B dye was measured by the characteristic absorption peak of rhodamine B at 554 nm.

## Results and discussion

### Morphological and structural analysis

Both the morphology and pore diameter of sphere-like SBA-15, as well as location of SnO<sub>2</sub>, TiO<sub>2</sub> and Sn<sub>0.25</sub>Ti<sub>0.75</sub>O<sub>2</sub> solid-solution- nanoparticles inside the mesopores of sphere-like SBA-15 were investigated by SEM and TEM images, shown in Fig. 1. The most commonly obtained SBA-15 morphology in literature is fiber-like,<sup>45</sup> which has a long aspect ratio (length to diameter of SBA-15 particles) of 10 or more, leading to additional diffusional-resistance of reactants and products inside pores of the porous host. Therefore, it is necessary to reduce the diffusion path-length of dye molecules for its efficient uptake and release of products. In order to do so, a hydrophobic substance (mesitylene) was added during synthesis in the present work, after formation of the SBA-15 particle. It is believed that, mesitylene eventually surrounds the silica particles and restricts their growth.

Consequently, SBA-15 particles are found to be of sphere-like morphology (with an aspect ratio near unity) in low magnification SEM images (Fig. 1a and 1b), having mean diameter of 630 nm and a standard deviation of 85 nm. TEM image of sphere-like SBA-15 (Fig. 1c) particles show well-ordered cylindrical pores, which are orientated parallel to each other. The mean pore diameter calculated from many such TEM images is 7.1 nm, with a standard deviation of 0.4 nm.

Subsequently, metal oxide precursors (SnCl<sub>4</sub> and TTIP) were allowed to impregnate under vacuum, to diffuse inside the pores of sphere-like SBA-15, in order to form corresponding metal oxide particles (SnO<sub>2</sub> and TiO<sub>2</sub> respectively). For Sn<sub>x</sub>Ti<sub>1-x</sub>O<sub>2</sub> solid-solution, different amounts of SnCl<sub>4</sub> and TTIP precursors were added together, which would diffuse inside the pores. This alters the atomic ratio of Sn and Ti, and provides the optimum composition with respect to the maximum photocatalytic activity against rhodamine B dye. To gain physical insight into photocatalysis, pure SnO<sub>2</sub> and pure TiO<sub>2</sub> nanoparticles were also embedded inside the pores of sphere-like SBA-15, as a control sample (Fig. 1d and 1e). A representative HRTEM image of SnO<sub>2</sub>-sphere-like SBA-15 is

shown in Fig. 1d. It is seen that, SnO<sub>2</sub> nanoparticles are well dispersed inside the pores, without any pore blockage. The measured mean diameter of SnO<sub>2</sub> particle from HRTEM images of SnO<sub>2</sub>- sphere-like SBA-15 is found to be 5.6 nm with a standard deviation of 0.9 nm.

Fig. 1e shows the dark field HRTEM image of TiO<sub>2</sub>-sphere-like SBA-15. It is difficult to locate TiO<sub>2</sub> nanoparticles inside the pores, in the bright field imaging mode, due to minimal difference in their atomic numbers. As shown in Fig. 1e, the measured mean diameter of TiO<sub>2</sub> nanoparticle is 5.8 nm. In case of Sn<sub>x</sub>Ti<sub>1-x</sub>O<sub>2</sub>-sphere-like SBA-15 samples (Fig. 1f), with increase in atomic percentage of Sn, nanoparticle size first decreases and then increases. The possible reason for reduction in solid-solution particle size (Table 1) is due to the introduction of strain in the crystal, on replacement of Ti<sup>4+</sup> with Sn<sup>4+</sup>.<sup>28</sup>

Peaks in wide angle X-ray diffraction (Fig. 2) in the SnO<sub>2</sub>-sphere-like SBA-15 sample can be indexed to the cassiterite tetragonal structure of crystalline SnO<sub>2</sub> (JCPDS No.: 41-1445). The mean SnO<sub>2</sub> from Scherrer's formula was found to be 6.7 nm, which is close to the value (5.6 nm), measured from TEM images. Similarly, peaks in TiO<sub>2</sub>- sphere-like SBA-15 can be assigned to the anatase phase [JCPDS card No. 21-1272]. Moreover, there are no peaks of other phases (rutile) in the sample, which confirms the presence of only pure anatase. The mean TiO<sub>2</sub> particle diameter of TiO<sub>2</sub> in sphere-like SBA-15 is 6.2 nm, which is close to the particle diameter (5.8 nm), measured from TEM images.

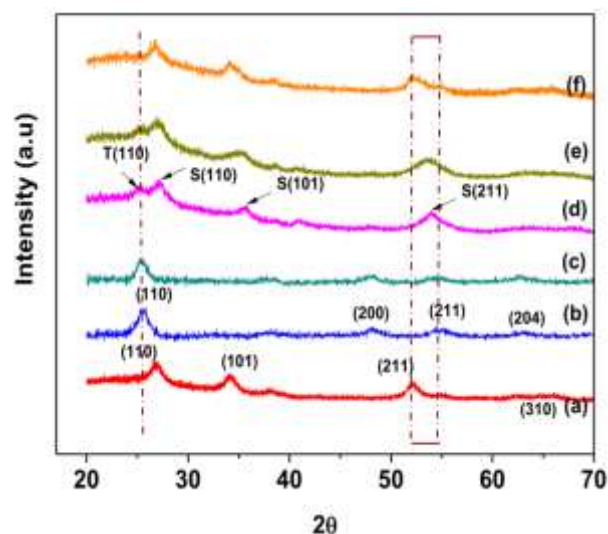


**Fig. 2** XRD spectra of (a) SnO<sub>2</sub>-sphere-like SBA-15, (b) TiO<sub>2</sub>-sphere-like SBA-15, (c) Sn<sub>0.05</sub>Ti<sub>0.95</sub>O<sub>2</sub>-sphere-like SBA-15, (d) Sn<sub>0.15</sub>Ti<sub>0.85</sub>O<sub>2</sub>-sphere-like SBA-15, (e) Sn<sub>0.25</sub>Ti<sub>0.75</sub>O<sub>2</sub>-sphere-like SBA-15, and (f) Sn<sub>0.50</sub>Ti<sub>0.50</sub>O<sub>2</sub>-sphere-like SBA-15. Rectangular bar shows changes in peak position when different percentages of Sn<sup>4+</sup> are embedded in the lattice of Ti<sup>4+</sup>.

After introduction of Sn in Sn<sub>x</sub>Ti<sub>1-x</sub>O<sub>2</sub>-sphere-like SBA-15, X-ray diffraction pattern shows several new peaks confirming the presence of titania (anatase phase) along with the minor tin oxide phase, which is in good agreement with literature.<sup>28</sup> From diffraction patterns (c-f) in Fig. 2, the diffraction peaks of

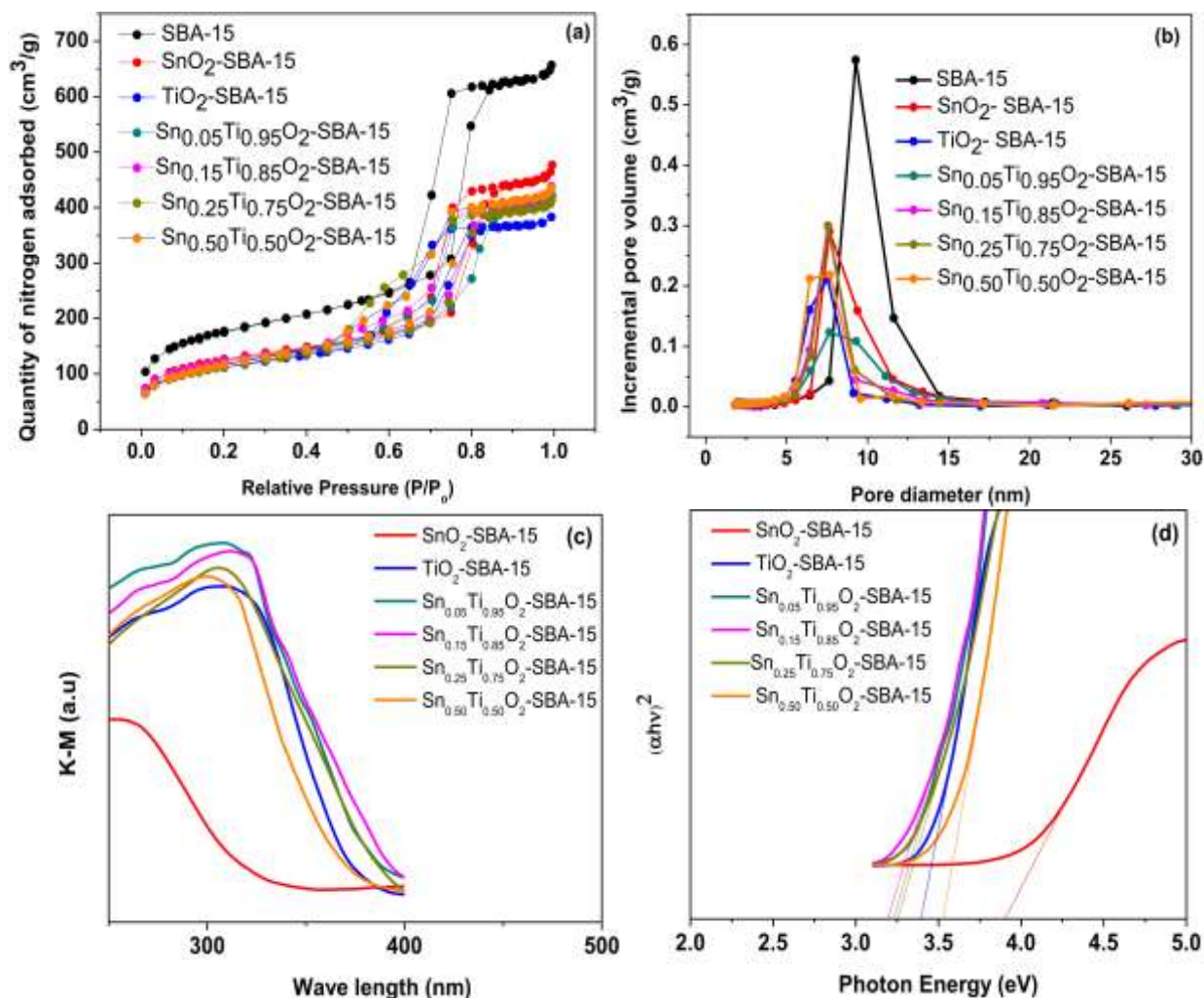
**Table 1** Textural and band gap properties of sphere-like SBA-15, SnO<sub>2</sub>-sphere like SBA-15, TiO<sub>2</sub>-sphere like SBA-15 and Sn<sub>x</sub>Ti<sub>1-x</sub>O<sub>2</sub>-sphere-like SBA-15.

Samples	Specific Surface area (m <sup>2</sup> /g)	Pore Volume (cm <sup>3</sup> /g)	Mean Pore Diameter	Mean nanoparticle size by XRD (nm)	Sn/(Sn+Ti)		Band gap (eV)
					Mean	Std dev	
Sphere-like SBA-15	640	1.05	9.1	NA	NA	NA	NA
SnO <sub>2</sub> -sphere-like SBA-15	448	0.71	7.7	6.7	NA	NA	3.90
TiO <sub>2</sub> -sphere-like SBA-15	409	0.62	7.7	6.2	NA	NA	3.39
Sn <sub>0.05</sub> Ti <sub>0.95</sub> O <sub>2</sub> -sphere-like SBA-15	420	0.65	7.5	5.6	0.05	0.02	3.23
Sn <sub>0.15</sub> Ti <sub>0.85</sub> O <sub>2</sub> -sphere-like SBA-15	428	0.68	7.6	4.3	0.14	0.01	3.19
Sn <sub>0.25</sub> Ti <sub>0.75</sub> O <sub>2</sub> -sphere-like SBA-15	411	0.64	7.6	3.3	0.24	0.01	3.25
Sn <sub>0.50</sub> Ti <sub>0.50</sub> O <sub>2</sub> -sphere-like SBA-15	424	0.67	7.7	6.0	0.51	0.01	3.52

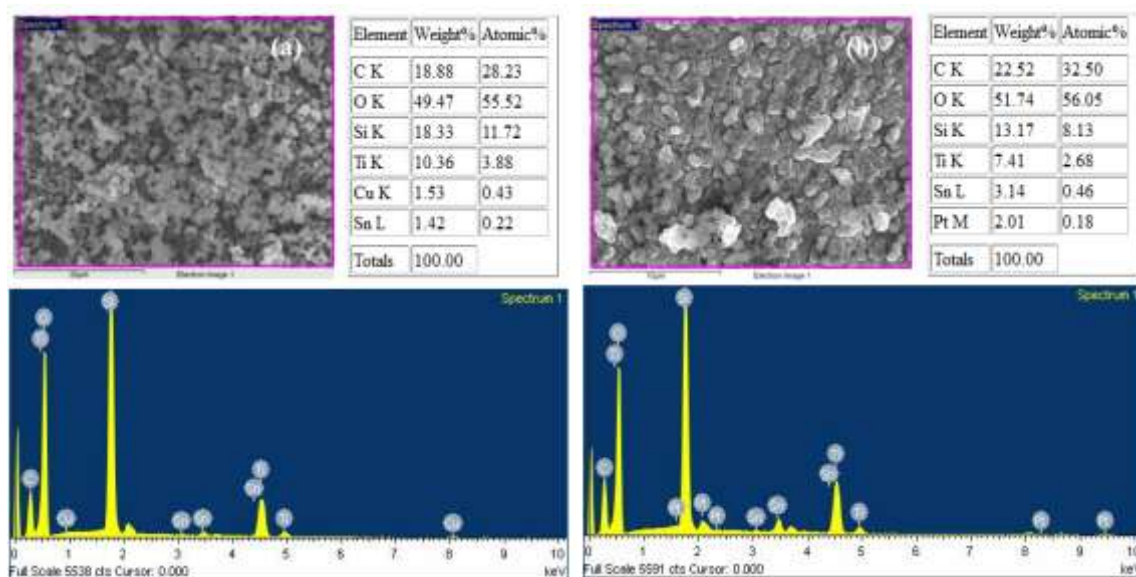
solid-solution samples are located between the pure SnO<sub>2</sub> and the pure TiO<sub>2</sub> peaks. However, upon increasing Sn amount in the Sn<sub>x</sub>Ti<sub>1-x</sub>O<sub>2</sub>-sphere-like SBA-15, the mean particle size is found to be 5.6, 4.3, and 3.3 nm for solid-solution samples with 5, 15 and 25 at.% Sn, respectively. This shows a decreasing trend in particle size with increase in Sn amount from 5-25 at.% Sn, which could be due to the strain arising from the replacement of Ti<sup>4+</sup> with Sn<sup>4+</sup>. Furthermore, it is noticed that there is an increase in peak broadening upon increased SnO<sub>2</sub> amount, which indicates a reduction in particle size.

It is seen from Fig. 3a that sphere-like SBA-15 particles have type IV adsorption isotherm with hysteresis loop, which confirms the presence of mesopores. Furthermore, capillary condensation is observed in the relative pressure range of 0.45-0.9, suggesting that the mesostructure has been retained in the sample. Features of sphere-like SBA-15 in terms of porous nature do not change after loading with SnO<sub>2</sub>, TiO<sub>2</sub> or Sn<sub>x</sub>Ti<sub>1-x</sub>O<sub>2</sub> particles. Moreover, there is a shift in lower relative pressure in nanoparticles loaded samples, as compared to pure sphere-like SBA-15, which indicates the reduction in mean pore size, due to the presence of nanoparticles. This observation is consistent with the pore size distribution plot as shown in Fig. 3b. The mean pore diameter, specific surface area and specific pore volume results are listed for all samples in Table 1. As shown in Table 2, specific surface area and mean pore diameter of nanoparticles embedded in sphere-like SBA-15 is in the range of 409-448 m<sup>2</sup>/g and 7.5-7.7 nm, respectively, which is less than that of pure sphere-like SBA-15 particles. This indirectly confirms the presence of nanoparticle inside the pores of the hybrid.

Diffuse reflectance UV-Vis spectra were recorded for all hybrid samples (Fig. 3c and 3d) to calculate band gap values (Table 1) and understand its influence on the photocatalytic performance. The band gap value is obtained by extrapolating the linear portion of the  $(ah\nu)^2$  versus photon energy (eV). Moreover, it is observed that there is a red shift of absorption edge in case of solid-solution particles embedded sphere-like SBA-15 in comparison to SnO<sub>2</sub>-sphere-like SBA-15, which shows the electronic structure of solid-solution particle has been altered. The reduction in band gap values (Table 1) after addition of Sn shows that the hybrids are not a simple mixture of SnO<sub>2</sub> and TiO<sub>2</sub>, but they are solid-solution. Furthermore, band gap value of TiO<sub>2</sub>-sphere-like SBA-15 (3.39 eV) is higher than that of Sn<sub>x</sub>Ti<sub>1-x</sub>O<sub>2</sub>- sphere-like SBA-15 (3.23, 3.19 and 3.25 eV for  $x = 0.05, 0.10$  and  $0.15$ , respectively), which indicates that the solid-solution sample has narrow band gap. This phenomenon will eventually results in promoting more charge carriers from the surface of photocatalyst. The band gap value increases further from 3.25 to 3.52eV when the value of  $x$  in Sn<sub>x</sub>Ti<sub>1-x</sub>O<sub>2</sub>-sphere-like SBA-15 increases from 0.25 to 0.50. Therefore, there could be a drastic change in reduction of photocatalytic activity in comparison with only TiO<sub>2</sub>-sphere-like SBA-15. The percentage of elements present in the hybrid is measured by EDX analysis and shown in Table 1. EDX spectra of all hybrids show the presence of both Sn and Ti in the Sn<sub>x</sub>Ti<sub>1-x</sub>O<sub>2</sub>-sphere-like SBA-15 samples. Fig. 4 and Table 1 shows that the atomic ratios from EDX spectra for all samples are very close to the atomic ratio added stoichiometrically during the synthesis. This confirms complete conversion of both Sn and Ti precursors into respective oxides.



**Fig. 3** (a) Nitrogen adsorption and desorption isotherm and (b) Pore size distribution of sphere-like SBA-15, SnO<sub>2</sub>- sphere-like SBA-15, TiO<sub>2</sub>-sphere-like SBA-15, and Sn<sub>x</sub>Ti<sub>1-x</sub>O<sub>2</sub>-sphere-like SBA-15 (c) Diffuse reflectance spectra and (d) Plots of the  $(\alpha hu)^2$  vs the photon energy of SnO<sub>2</sub>-sphere-like SBA-15, TiO<sub>2</sub>-sphere-like SBA-15 and Sn<sub>x</sub>Ti<sub>1-x</sub>O<sub>2</sub>-sphere-like SBA-15.



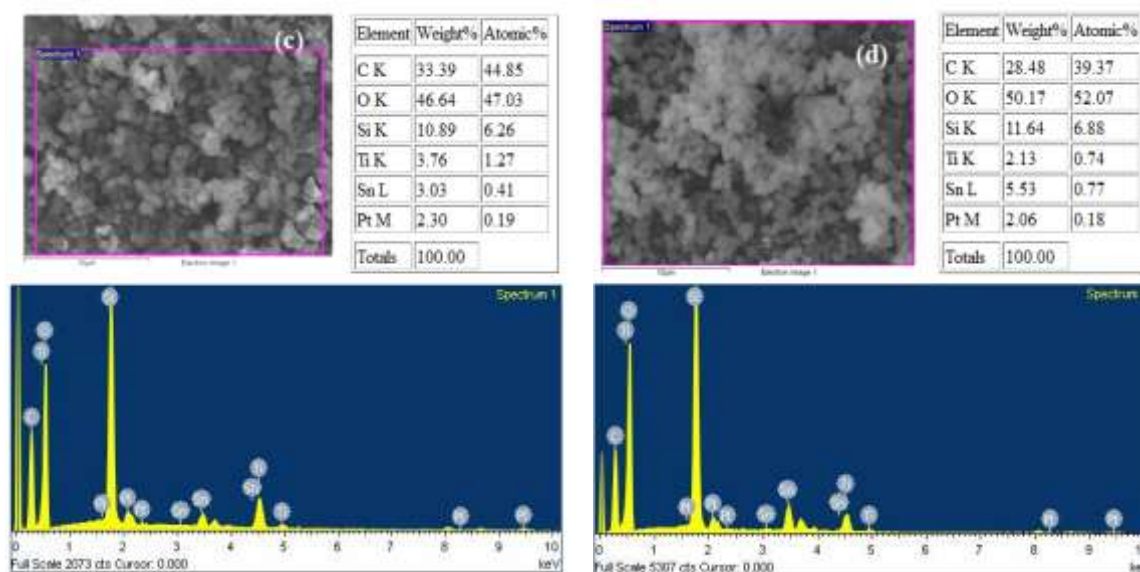


**Fig. 4** EDX spectra of (a)  $\text{Sn}_{0.05}\text{Ti}_{0.95}\text{O}_2$ -sphere-like SBA-15, (b)  $\text{Sn}_{0.15}\text{Ti}_{0.85}\text{O}_2$ -sphere-like SBA-15, (c)  $\text{Sn}_{0.25}\text{Ti}_{0.75}\text{O}_2$ -sphere-like SBA-15, and (d)  $\text{Sn}_{0.50}\text{Ti}_{0.50}\text{O}_2$ -sphere-like SBA-15. Rectangular bar in SEM images are the areas selected for elemental analysis.

The percentage of photocatalyst in the final samples for all the hybrids was kept same at 17.7 wt.%.

#### Photocatalytic activity of $\text{Sn}_x\text{Ti}_{1-x}\text{O}_2$ -sphere-like SBA-15

To investigate the photocatalytic activity, rhodamine B dye was allowed to react with  $\text{Sn}_x\text{Ti}_{1-x}\text{O}_2$ -sphere-like SBA-15 under UV light. The change in concentration of rhodamine B as a function of irradiation time in presence of different atomic percentages (5, 15, 25, and 50 %) of Sn in  $\text{Sn}_x\text{Ti}_{1-x}\text{O}_2$ -sphere-like SBA-15,  $\text{SnO}_2$ -SBA-15 and  $\text{TiO}_2$ -SBA-15 is shown in Fig. 5. A pseudo-first order dye degradation equation,  $-\ln(C/C_0) = kt$ , was used for calculating the first order rate constant ( $k$ ) for all hybrid samples, where  $C$  and  $C_0$  are dye concentrations at any later time  $t$ , and at initial time,  $t = 0$ , respectively. As seen in Fig. 5, the photocatalytic activity of  $\text{SnO}_2$ -sphere-like SBA-15 ( $k = 0.14 \text{ h}^{-1}$ ) is much less compared to  $\text{TiO}_2$ -sphere-like SBA-15 ( $k = 1.38 \text{ h}^{-1}$ ).

This is because of wide band gap of  $\text{SnO}_2$ -sphere-like SBA-15 (3.9 eV, from Table 1), leading to a limited absorption of photons. On the other hand,  $\text{TiO}_2$ -sphere-like SBA-15 has a narrower band gap (3.39 eV, from Table 1), which results in a much better photocatalytic activity. When the amount of Sn was slowly increased, it was found that the sample with 5 at.% of Sn ( $\text{Sn}_{0.05}\text{Ti}_{0.95}\text{O}_2$ -sphere-like SBA-15) showed even better photocatalytic activity ( $1.86 \text{ h}^{-1}$ ) than that of pure  $\text{TiO}_2$ -sphere-like SBA-15 ( $k = 1.38 \text{ h}^{-1}$ ). However, the photocatalytic activity decreased slowly with further increase in atomic percentage of Sn in the hybrid. The photocatalytic activity of a semiconductor is also dependent on charge carrier transfer and its separation efficiency. To this end, electrochemical impedance spectrum (EIS) was measured in order to understand these aspects at the interface of a semiconductor

particle.<sup>46</sup> The Nyquist plot of the EIS measurement for all samples is shown in Fig. 6a. The equivalent-circuit model is also fitted for all EIS spectra (Fig. 6a), where  $R_s$  is the solution resistance,  $R_{ct}$  is the charge transfer resistance, and  $C_{dl}$  is the double layer capacitance. To gain further insight on charge transport and recombination kinetics, model parameters were calculated using the Zsimp win software and are listed in Table 2.

In general, the electron-transfer behaviour of the samples is reflected by the arc of the spectrum. The smaller arc in EIS spectra indicates an effective separation of charge carriers and a faster interfacial charge transfer. It is seen from Fig. 6 that the arc of  $\text{Sn}_{0.05}\text{Ti}_{0.95}\text{O}_2$ -sphere-like SBA-15 is much smaller than  $\text{SnO}_2$ -sphere-like SBA-15 or  $\text{TiO}_2$ -sphere-like SBA-15, suggesting lower the electron transfer resistance and faster interfacial charge transfer rate in the former. The arc slowly vanishes as the loading of Sn increases, which suggests that charge transfer resistance increases.

**Table 2** Model Parameters of all hybrids based on EIS results

Sample	Solution resistance $R_s$ ( $\Omega \text{ cm}^{-2}$ )	Charge Transfer Resistance $R_{ct}$ ( $\text{K}\Omega \text{ cm}^{-2}$ )	Double layer capacitance $C_{dl}$ ( $\mu\text{F cm}^{-2}$ )
$\text{SnO}_2$ -SBA-15	68.1	8920	3.32
$\text{TiO}_2$ -SBA-15	67.4	910	5.71
$\text{Sn}_{0.05}\text{Ti}_{0.95}\text{O}_2$ -SBA-15	67.7	332	6.10
$\text{Sn}_{0.15}\text{Ti}_{0.85}\text{O}_2$ -SBA-15	65.4	1236	5.28
$\text{Sn}_{0.25}\text{Ti}_{0.75}\text{O}_2$ -SBA-15	66.2	1798	4.97
$\text{Sn}_{0.50}\text{Ti}_{0.50}\text{O}_2$ -SBA-15	67.1	2300	4.68

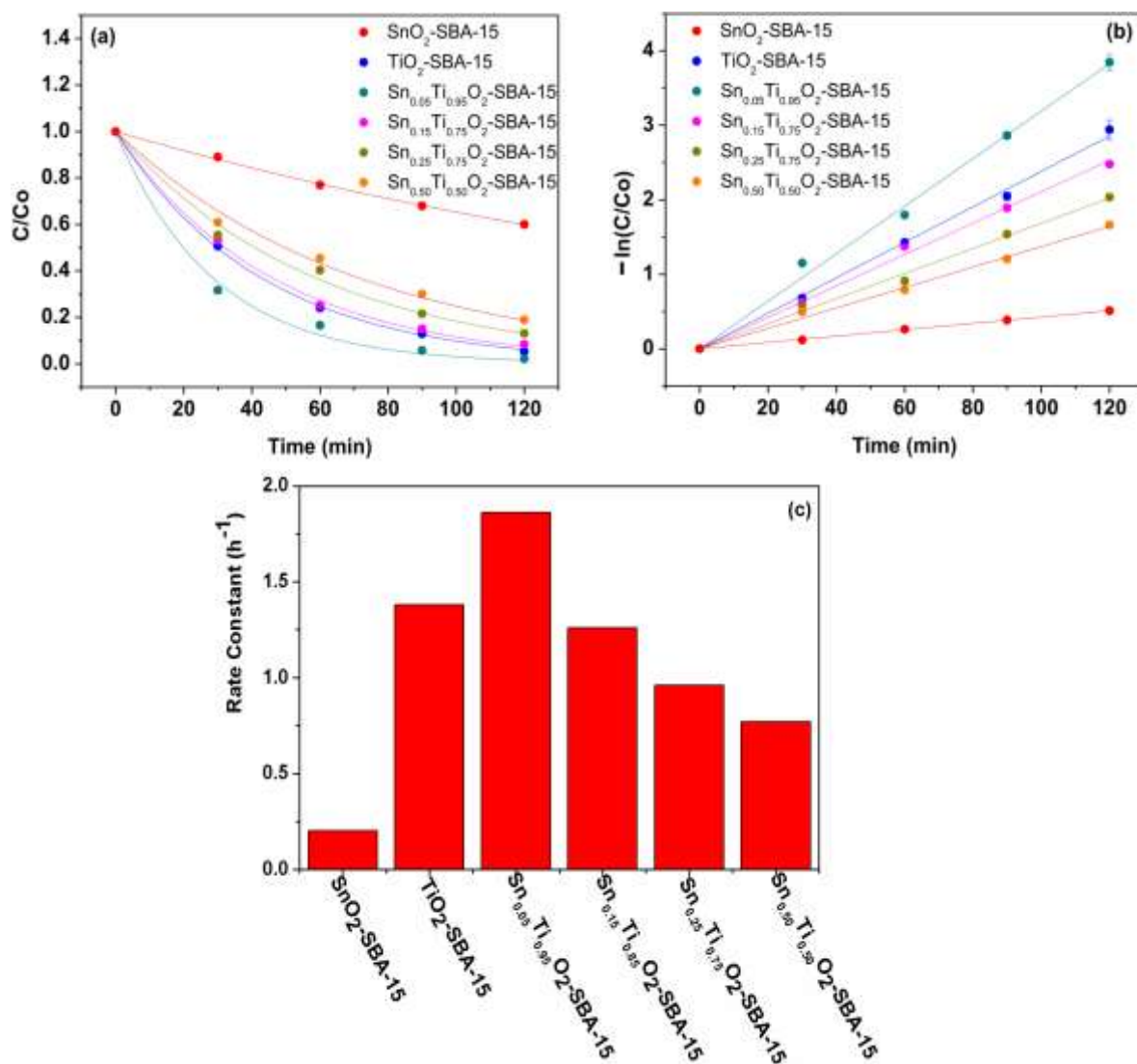


Fig. 5 (a) Normalized concentration profile of rhodamine B dye with UV irradiation time for different photocatalysts (b) Comparison of experiments with fitted kinetics of rhodamine B dye for different photocatalysts (c) Effect of Sn content in  $\text{Sn}_x\text{Ti}_{1-x}\text{O}_2$ -sphere-like SBA-15 on degradation rate constant.

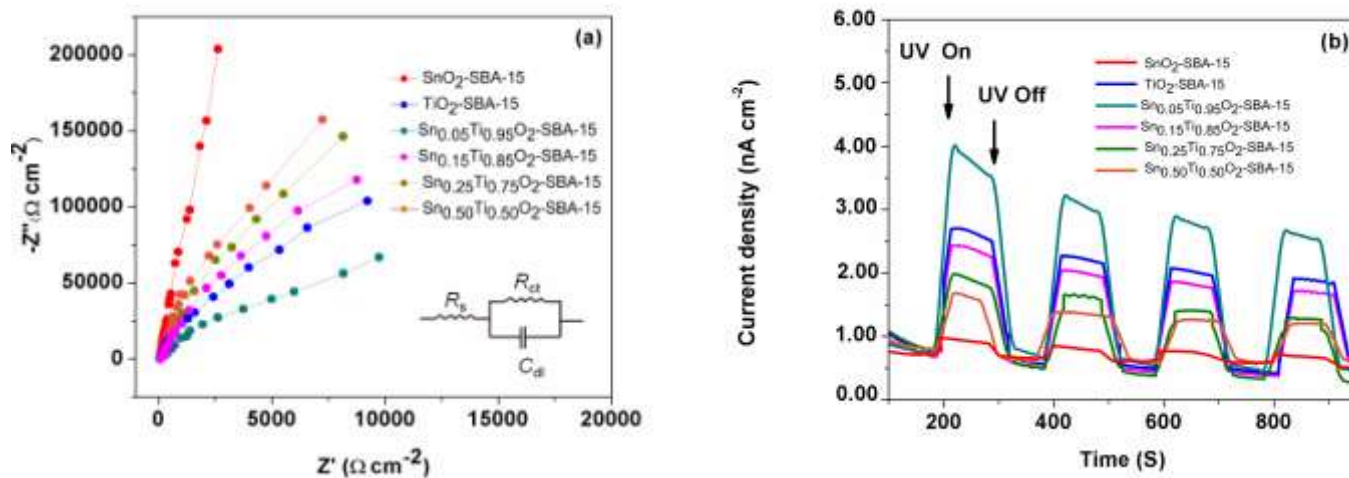


Fig. 6. (a) Nyquist plots and (b) Transient photocurrent responses of  $\text{SnO}_2$ -sphere-like SBA-15,  $\text{TiO}_2$ - sphere-like SBA-15,  $\text{Sn}_{0.05}\text{Ti}_{0.95}\text{O}_2$ - sphere-like SBA-15,  $\text{Sn}_{0.15}\text{Ti}_{0.85}\text{O}_2$ -sphere-like SBA-15,  $\text{Sn}_{0.25}\text{Ti}_{0.75}\text{O}_2$ - sphere-like SBA-15 and  $\text{Sn}_{0.50}\text{Ti}_{0.50}\text{O}_2$ -sphere-like SBA-15.

From Table 2, it can be seen that the solution resistance ( $R_s$ ) value for all hybrids is almost same. The charge transfer resistance ( $R_{ct}$ ) however decreases from  $910 \text{ K}\Omega \text{ cm}^{-2}$  to  $332 \text{ K}\Omega \text{ cm}^{-2}$ , on addition of 5 at.% of Sn in the  $\text{TiO}_2$  matrix, which could be due to the increase in faradic current, as a result of reduction in recombination of charge carriers. Overall, solid-solution in sphere-like SBA-15 reduces the recombination of charge carriers, resulting in superior photocatalytic activity.

Photocurrent responses (Fig. 6b) were recorded for few on-off cycles of UV irradiation. The value of photocurrent will quickly go down to zero once the UV light is switched off, whereas it will return to a steady value, when the light is again turned on. The above trend is reproducible and shows stability over a few cycles. The  $\text{Sn}_{0.05}\text{Ti}_{0.95}\text{O}_2$ -sphere-like SBA-15 shows much higher photocurrent intensity than other hybrids, indicating that the sample can reduce charge carrier recombination, by improving interfacial charge transfer under UV irradiation.

For gaining further insight into the maximum enhancement of photocatalytic activity in the  $\text{Sn}_{0.05}\text{Ti}_{0.95}\text{O}_2$ -sphere-like SBA-15 sample, compared to  $\text{TiO}_2$ -sphere-like SBA-15 - so as to emphasize the role of surface states - XPS spectra of both samples are compared in Fig.S1 (ESI<sup>+</sup>). This confirms the presence of elements and chemical states. Fig.S1 shows spectra from XPS of the complete survey of elements (Fig. S1a, ESI<sup>+</sup>), Ti2p (Fig. S1b, ESI<sup>+</sup>) and O1s (Fig. S1c and d, ESI<sup>+</sup>). The complete survey (Fig. S1a, ESI<sup>+</sup>) shows the presence of Sn, Ti, C, Si and O elements in  $\text{Sn}_{0.05}\text{Ti}_{0.95}\text{O}_2$ -sphere-like SBA-15, while Ti, C, Si and O elements occur in  $\text{TiO}_2$ -sphere-like SBA-15, respectively. The presence of elemental C in both samples could be due to atmospheric contamination during sample exposure in air.<sup>47</sup> Fig S1b (ESI<sup>+</sup>) shows the high resolution spectra of Ti 2p region, for both samples at about 458.8 and 464.6 eV corresponding to Ti 2p<sub>3/2</sub> and Ti 2p<sub>1/2</sub>. The two peaks of the Ti2p for the  $\text{Sn}_{0.05}\text{Ti}_{0.95}\text{O}_2$ -sphere-like SBA-15 show a slight shift towards higher binding energy levels, in comparison to  $\text{TiO}_2$ -sphere-like SBA-15.<sup>48,49</sup> This is mainly due to the variation of electronegativities of Ti and Sn elements (Ti - 1.54 and Sn - 1.96) and confirms the bonding of Ti-O-Sn in  $\text{Sn}_{0.05}\text{Ti}_{0.95}\text{O}_2$ -sphere-like SBA-15. Furthermore, the position of Ti 2p doublet peaks and the splitting value of 5.8 eV indicate the presence of  $\text{Ti}^{4+}$  oxidation state. In order to quantify oxygen vacancies in both samples, O 1s peak (Fig. S1c, ESI<sup>+</sup>) was deconvoluted into three peaks at about 530.1, 531.5 and 532.5 eV, which are associated with lattice oxygen species ( $\text{O}_l$ ), oxygen vacancies ( $\text{O}_v$ ) and hydroxyl oxygen species ( $\text{O}_h$ ), respectively. The percentages of  $\text{O}_v$  (10.85 %) and  $\text{O}_h$  (63.53 %) were increased for  $\text{Sn}_{0.05}\text{Ti}_{0.95}\text{O}_2$ -sphere-like SBA-15, compared to  $\text{TiO}_2$ -sphere-like SBA-15 ( $\text{O}_v$  (8.35%) and  $\text{O}_h$  (61.57 %)). The increase in oxygen vacancy is the result of substitution of  $\text{Sn}^{4+}$  in  $\text{Ti}^{4+}$  lattice due to the weakening of Ti-O bonds.

To explore the possible mechanism of higher photodegradation by  $\text{Sn}_{0.05}\text{Ti}_{0.95}\text{O}_2$ -sphere-like SBA-15 hybrid compared to other samples, their band positions were calculated from Mulliken electronegativity, using the following empirical formulae.<sup>50,51</sup>

$$E_{VB} = X - E_e + 0.5 E_g \quad (1)$$

$$E_{CB} = E_{VB} - E_g \quad (2)$$

where,  $E_{VB}$  represents valence band edge potential,  $E_{CB}$  represents conduction band edge potential,  $E_g$  represents the band gap energy of the semiconductor,  $E_e$  is the energy of free electrons on the hydrogen scale (4.5 eV), and  $X$  is the electronegativity of the semiconductor, which is calculated based on the arithmetic mean of the atomic electron affinity and the ionization potential. The calculated values of  $X$ ,  $E_{CB}$ , and  $E_{VB}$  are given in Table 3.

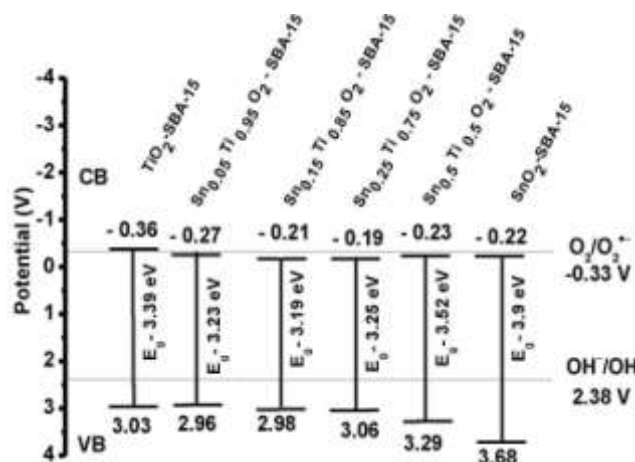


**Fig. 7** Schematic energy level diagram of  $\text{Sn}_x\text{Ti}_{1-x}\text{O}_2$ -sphere-like SBA-15 hybrids.

**Table 3** Calculated values of  $X$ ,  $E_{VB}$ , and  $E_{CB}$  for  $\text{Sn}_x\text{Ti}_{1-x}\text{O}_2$ -sphere-like SBA-15 hybrids.

Sample	$X$ (eV)	$E_{VB}$ (eV)	$E_{CB}$ (eV)
$\text{TiO}_2$ -SBA-15	5.83	3.03	-0.36
$\text{Sn}_{0.05}\text{Ti}_{0.95}\text{O}_2$ -SBA-15	5.85	2.96	-0.27
$\text{Sn}_{0.15}\text{Ti}_{0.85}\text{O}_2$ -SBA-15	5.89	2.98	-0.21
$\text{Sn}_{0.25}\text{Ti}_{0.75}\text{O}_2$ -SBA-15	5.93	3.06	-0.19
$\text{Sn}_{0.50}\text{Ti}_{0.50}\text{O}_2$ -SBA-15	6.03	3.29	-0.23
$\text{SnO}_2$ -SBA-15	6.23	3.68	-0.22

Based on the energy band structure calculation, the energy level diagram for all hybrids is shown in Fig 7. This band energy structure calculation is necessary as the redox ability of the photogenerated electron-hole pairs depends on the band position of the semiconductor. The conduction band and valence band potentials of  $\text{Sn}_x\text{Ti}_{1-x}\text{O}_2$  sphere-like SBA-15 hybrid are positioned between the  $\text{SnO}_2$ -sphere-like SBA-15 and  $\text{TiO}_2$ -sphere-like SBA-15. It is clearly seen that potentials can be adjusted by changing the ratio of Sn and Ti in the hybrid. It has been found that the values of redox couples ( $\text{OH}^\bullet/\text{OH}$  and  $\text{O}_2/\text{O}_2^{\bullet-}$ ) display the potential (vs SHE) of 2.38 and -0.33V, respectively.<sup>52</sup> These potential values are considered as the

**Table 4** Comparison of photocatalytic performance of  $\text{Sn}_x\text{Ti}_{1-x}\text{O}_2$ -SBA-15 hybrid with similar reports based on  $\text{SnO}_2$  and  $\text{TiO}_2$ .

Sl. no.	Photocatalyst	Rhodamine B dye concentration ( $\mu\text{M}$ )	Catalyst (%)	Degradation time (min.)	Rate constant ( $\text{h}^{-1}$ )	Reference no.
1	$\text{SnO}_2$	10	100	150	0.20	4
2.	$\text{SnO}_2$ -SBA-15	50	5	600	0.067, 0.14	33
3.	$\text{SnO}_2$ -SBA-15	50	5	360	0.54	34
4	$\text{TiO}_2$	10	100	180	0.43	28
5	$\text{TiO}_2$ -SBA-16	10	5	120	1.63	39
6	$\text{TiO}_2$ -SBA-15	50	17.7	120	1.38	Present work
7	$\text{SnO}_2$ - $\text{TiO}_2$	20	100	60	0.91	48
8	$\text{SnO}_2$ - $\text{TiO}_2$	10	100	180	0.73	28
9	$\text{Sn}_{0.05}\text{Ti}_{0.95}\text{O}_2$ -SBA-15	50	17.7	120	1.86	Present work

conduction and valence band positions, if radicals are present in the system.

From Fig. 7, valence band of  $\text{Sn}_x\text{Ti}_{1-x}\text{O}_2$ -sphere-like SBA-15 is more positive than that of  $\text{E}^\bullet$  ( $\text{OH}^\bullet/\text{OH}^-$ ) (2.38 V vs SHE). As a result, the most prominent way of degradation could be the oxidation of  $\text{OH}^-$  to  $\text{OH}^\bullet$  by photogenerated holes, rather than the reduction of  $\text{O}_2$  to  $\text{O}_2^{\bullet-}$  by photogenerated electrons. Furthermore, the addition of Sn in  $\text{TiO}_2$  matrix ( $\text{Sn}_{0.05}\text{Ti}_{0.95}\text{O}_2$ -sphere-like SBA-15) decreases the conduction band and valence band potential, which is less than that of pure  $\text{TiO}_2$ -sphere-like SBA-15. This leads to a narrow band gap and reduction in recombination of charge carriers, thereby increasing the photocatalytic activity of the sample. However, addition of Sn with 15, 25 and 50 at.% in the hybrid leads to reduction in photocatalytic activity. The possible reason for this could be due to the appearance of more crystalline features of  $\text{SnO}_2$  and prevention or delay of crystallization of  $\text{TiO}_2$  phase in the solid-solution. The other reasons may be due to the formation of  $\text{SnO}_2$  arising from the non-substituted  $\text{Sn}^{4+}$  in the crystal lattice of solid-solution-nanoparticles and increase in band gap values. Thus, based on the photocatalytic activity in this work, maximum percentage of Sn to be used in  $\text{Sn}_x\text{Ti}_{1-x}\text{O}_2$  is 5 at.%. The narrow band gap due to band structure modification is also supported by photoluminescence (Fig. S2, ESI<sup>†</sup>), which is mainly the result of recombination of charge carriers. The sample ( $\text{Sn}_{0.05}\text{Ti}_{0.95}\text{O}_2$ -sphere-like SBA-15) is less luminescent in comparison to  $\text{TiO}_2$ -sphere-like SBA-15. The possible reason is the presence of oxygen vacancies and consequent reduction of recombination of charge of carriers.<sup>53</sup> Therefore, photocatalytic mechanism of  $\text{Sn}_x\text{Ti}_{1-x}\text{O}_2$ -sphere-like SBA-15 is explained by surface states, electronic structure, luminescence and charge carriers transfer at the interface by EIS.

Table 4 shows a comparison of recent studies on photodegradation of dye by  $\text{Sn}_x\text{Ti}_{1-x}\text{O}_2$ -sphere-like SBA-15, with different forms of  $\text{SnO}_2$ - $\text{TiO}_2$  hybrids. The goal is to identify important parameters such as, catalyst loading, degradation

time etc. Other than the effect of nanoparticle composition (shown in this work), factors such as pore blockage and SBA-15 morphology (geometrical features) of the porous host also play an important role in enhancing photodegradation. For example, removal of pore blockage (by reducing the embedded  $\text{SnO}_2$  nanoparticle size from 6.8 to 3.5 nm) in  $\text{SnO}_2$ -fiber-like SBA-15 increased the first order degradation rate constant from 0.067 to 0.14  $\text{h}^{-1}$  (Table 4, sl. No. 2) - about 2.1 times - emphasizing the need for smaller-sized embedded nanoparticles. Similarly, reducing the aspect ratio by changing the SBA-15 particle's external morphology from fiber-like (aspect ratio  $\sim 11$ ) to sphere-like (aspect ratio  $\sim 1$ ), further improved the rate constant by a factor of 3.8 from 0.14 to 0.54  $\text{h}^{-1}$  (Table 4, sl. No. 3). Incorporating these improvements and pushing further in the present work, the optimum composition (of  $x = 0.05$ ) in  $\text{Sn}_x\text{Ti}_{1-x}\text{O}_2$  achieved a very significant increase in the rate constant, from 0.54 to 1.86  $\text{h}^{-1}$ , *i. e.* by an additional factor of 3.4. Therefore, embedding of solid-solution-nanoparticles inside a porous host (as shown in this work), together with ensuring of no-pore blockage (by using 5.6 nm diameter catalytic particles in 7 nm diameter SBA-15 host) and shorter pore-channel length (using sphere-like, short aspect ratio SBA-15 host) helped in achieving an overall very impressive rate improvement (from 0.067 to 1.86  $\text{h}^{-1}$ , a combined factor of about 27.8 times) in photocatalytic degradation.

It is further seen from Table 4 (sl. nos. 1 and 4) that, only  $\text{TiO}_2$  without any porous host ( $k = 0.43 \text{ h}^{-1}$ ) is a better photocatalyst in comparison to only  $\text{SnO}_2$  without any porous host ( $k = 0.20 \text{ h}^{-1}$ ), obviously because of the smaller band gap of the former. However, these materials perform far better when they are embedded in the porous SBA-15 matrix. The porous matrix increases the accessible specific surface area of the photocatalyst particles, by preventing nanoparticle inter-aggregation due to attractive surface forces. Therefore, values of  $k = 0.14 \text{ h}^{-1}$  and  $k = 1.38 \text{ h}^{-1}$  are obtained (sl. nos. 2 and 6 in Table 4) for pure  $\text{SnO}_2$ -SBA-15 and pure  $\text{TiO}_2$ -SBA-15,

respectively. Therefore, a further aspect of improvement is achieved when the two oxides are combined into a heterostructure, with rate constants ( $k = 0.73$  and  $0.91 \text{ h}^{-1}$ , sl. nos. 8 and 7 in Table 4, respectively), being better than that of individual oxide particles ( $k = 0.43 \text{ h}^{-1}$ , sl. no. 4 in Table 4). The decrease in recombination of charge carriers in the heterostructure could be the reason for such an improvement. Therefore, the enhancements obtained in the current work are from the following aspects: (i) using a porous host particle of nearly spherical shape (i. e. shorter pore-length to increase the accessibility of the nanoparticle surface by dye molecule) and to prevent pore blockage and (ii) using a combination of two oxides (in the form of a solid-solution in each nanoparticle). As a result,  $\text{Sn}_{0.05}\text{Ti}_{0.95}\text{O}_2$ -sphere-like SBA-15 ( $k = 1.86 \text{ h}^{-1}$ , sl. no. 9 in Table 4) provides the fastest rate of dye degradation than that of any other hybrid in Table 4. Furthermore, these changes in the hybrid will make an impact in the application of dye-sensitized solar cell (DSSC), where recombination of charge carriers is one of the loss factors. Another impact would be in application areas such as lithium-ion batteries and gas sensors, where transport of electrons in a short path length is important to enhance their performances. Presence of semiconductor nanoparticles along with the shorter length of a porous matrix results in a faster response, whenever it is exposed to diffusing molecules in a gas sensor or ions in a lithium-ion battery. Therefore, these functional differences can make an impact not only in the area of photocatalysis, but also in other areas where recombination of charge carriers and transport of electrons are important.

## CONCLUSIONS

In summary, this work demonstrates the formation of controlled  $\text{Sn}_x\text{Ti}_{1-x}\text{O}_2$  solid-solution-nanoparticles inside sphere-like SBA-15 particles. This ensures confinement of small oxide nanoparticles within the mesopores of SBA-15, without interparticle aggregation, thereby eliminating pore blockage. On varying  $x$  between 0 (pure  $\text{TiO}_2$ ) to 1.0 (pure  $\text{SnO}_2$ ) with other intermediate values, it is observed that the hybrid with 5 at.% of Sn, i.e.,  $\text{Sn}_{0.05}\text{Ti}_{0.95}\text{O}_2$ -SBA-15 shows the maximum photocatalytic activity for degradation of rhodamine-B dye (first order rate constant,  $k = 1.86 \text{ h}^{-1}$ ), compared to both pure  $\text{TiO}_2$ -sphere-like SBA-15 ( $k = 1.38 \text{ h}^{-1}$ ) or pure  $\text{SnO}_2$ -sphere-like SBA-15 ( $k = 0.14 \text{ h}^{-1}$ ). Electrochemical impedance spectroscopy shows increase in charge carrier lifetime to the maximum extent in  $\text{Sn}_{0.05}\text{Ti}_{0.95}\text{O}_2$ -sphere-like SBA-15, leading to enhanced photocatalytic activity of hybrid. This enhancement is well supported by XPS and PL spectra, showing the effect of increase in oxygen vacancies in  $\text{Sn}_{0.05}\text{Ti}_{0.95}\text{O}_2$ -SBA-15, compared to  $\text{TiO}_2$ -sphere-like SBA-15. However, further increase in Sn amount from 5 to 50 at.%, led to a reduction in photocatalytic activity, due to gradual loss of the anatase phase in  $\text{TiO}_2$ . Therefore,  $\text{Sn}_{0.05}\text{Ti}_{0.95}\text{O}_2$ -sphere-like SBA-15 displays the highest dye degradation rate constant because of its structural features (crystallinity, particle size, specific surface area) and electronic properties (band structure and

mobility of charge carriers) than that of previous reports based on only  $\text{SnO}_2$ , only  $\text{TiO}_2$  or other hybrids. This work not only demonstrates a methodology to form solid-solution nanoparticles of  $\text{SnO}_2$  and  $\text{TiO}_2$ , well-dispersed and embedded inside sphere-like SBA-15 particles without pore blockage, but also provides new insight into understanding the optimum atomic percentages of Sn and Ti in terms of their photocatalytic performance. Thus, as shown above in Table 4, optimization of geometrical structure and composition in any hybrid is crucial to achieve maximum rate enhancement in any heterogeneous catalytic reaction. Therefore, these findings can be translated to alter the electronic structure of semiconductor nanoparticles inside porous hosts (with maximum accessibility of nanoparticle surface), for even other different applications of hybrid materials, as in dye-sensitized solar cell, hydrogen production etc.

## Acknowledgements

Authors acknowledge National Centre for Nanoscience and Nanotechnology, University of Madras, Chennai, and Department of Chemistry, Indian Institute of Technology Madras for XPS and PL spectra, respectively.

## Notes and references

- 1 R. Asahi, T. Morikawa, T. Ohwaki, K. Aoki and Y. Taga, *Science*, 2001, **293**, 269–271.
- 2 A. Hagfeldt and M. Graetzel, *Chem. Rev.*, 1995, **95**, 49–68.
- 3 Z. Zou, J. Ye, K. Sayama and H. Arakawa, *Nature*, 2001, **414**, 625–627.
- 4 S. Wu, H. Cao, S. Yin, X. Liu and X. Zhang, *J. Phys. Chem. C*, 2009, **113**, 17893–17898.
- 5 G. Ciardelli and N. Ranieri, *Water Res.*, 2001, **35**, 567–572.
- 6 P. R. Gogate and A. B. Pandit, *Adv. Environ. Res.*, 2004, **8**, 501–551.
- 7 A. FUJISHIMA and K. HONDA, *Nature*, 1972, **238**, 37–38.
- 8 M. R. Hoffmann, S. T. Martin, W. Choi and D. W. Bahnemann, *Chem. Rev.*, 1995, **95**, 69–96.
- 9 Y. Qu and X. Duan, *Chem. Soc. Rev.*, 2013, **42**, 2568–2580.
- 10 H. Zhou, Y. Qu, T. Zeid and X. Duan, *Energy Environ. Sci.*, 2012, **5**, 6732.
- 11 B. Sun, A. V Vorontsov and P. G. Smirnotis, *Langmuir*, 2003, **19**, 3151–3156.
- 12 S. Sakthivel, M. V Shankar, M. Palanichamy, B. Arabindoo, D. W. Bahnemann and V. Murugesan, *Water Res.*, 2004, **38**, 3001–3008.
- 13 Z. Bian, T. Tachikawa, W. Kim, W. Choi and T. Majima, *J. Phys. Chem. C*, 2012, **116**, 25444–25453.
- 14 W. Choi, A. Termin and M. R. Hoffmann, *J. Phys. Chem.*, 1994, **98**, 13669–13679.

## ARTICLE

## Journal Name

- 15 S. G. Kumar and L. G. Devi, *J. Phys. Chem. A*, 2011, **115**, 13211–13241.
- 16 H. Yamashita, M. Harada, J. Misaka, M. Takeuchi, K. Ikeue and M. Anpo, *J. Photochem. Photobiol. A Chem.*, 2002, **148**, 257–261.
- 17 Q. Xiang, J. Yu, W. Wang and M. Jaroniec, *Chem. Commun.*, 2011, **47**, 6906–6908.
- 18 J. C. Yu, Yu, Ho, Jiang and Zhang, *Chem. Mater.*, 2002, **14**, 3808–3816.
- 19 M. Zhou and J. Yu, *J. Hazard. Mater.*, 2008, **152**, 1229–1236.
- 20 S. Sakthivel and H. Kisch, *Angew. Chemie Int. Ed.*, 2003, **42**, 4908–4911.
- 21 D. Kannaiyan, E. Kim, N. Won, K. W. Kim, Y. H. Jang, M.-A. Cha, D. Y. Ryu, S. Kim and D. H. Kim, *J. Mater. Chem.*, 2010, **20**, 677.
- 22 Z. Zhang, W. Wang, L. Wang and S. Sun, *ACS Appl. Mater. Interfaces*, 2012, **4**, 593–597.
- 23 K. Vinodgopal and P. V. Kamat, *Environ. Sci. Technol.*, 1995, **29**, 841–5.
- 24 A. Fontes Garcia, M. Fernandes and P. Coutinho, *Nanoscale Res. Lett.*, 2011, **6**, 426.
- 25 L. Lin, Y. Yang, L. Men, X. Wang, D. He, Y. Chai, B. Zhao, S. Ghoshroy and Q. Tang, *Nanoscale*, 2013, **5**, 588–593.
- 26 E. M. El-Maghraby, *Phys. B Condens. Matter*, 2010, **405**, 2385–2389.
- 27 Y. Wang, J. Wu, J. Zheng, R. Jiang and R. Xu, *Catal. Sci. Technol.*, 2012, **2**, 581–588.
- 28 M. F. Abdel-Messih, M. a. Ahmed and A. S. El-Sayed, *J. Photochem. Photobiol. A Chem.*, 2013, **260**, 1–8.
- 29 Y. Huang, Z. Zheng, Z. Ai, L. Zhang, X. Fan and Z. Zou, *J. Phys. Chem. B*, 2006, **110**, 19323–19328.
- 30 S. Ponja, S. Sathasivam, N. Chadwick, A. Kafizas, S. M. Bawaked, A. Y. Obaid, S. Al-Thabaiti, S. N. Basahel, I. P. Parkin and C. J. Carmalt, *J. Mater. Chem. A*, 2013, **1**, 6271–6278.
- 31 M. Liu, L. Wang, G. (Max) Lu, X. Yao and L. Guo, *Energy Environ. Sci.*, 2011, **4**, 1372–1378.
- 32 M. V. Phanikrishna Sharma, V. Durga Kumari and M. Subrahmanyam, *Chemosphere*, 2008, **73**, 1562–1569.
- 33 N. R. Srinivasan and R. Bandyopadhyaya, *Microporous Mesoporous Mater.*, 2012, **149**, 166–171.
- 34 N. R. Srinivasan, P. Majumdar, N. K. R. Eswar and R. Bandyopadhyaya, *Applied Catal. A, Gen.*, 2015, **498**, 107–116.
- 35 T. Kamegawa, R. Kido, D. Yamahana and H. Yamashita, *Microporous Mesoporous Mater.*, 2013, **165**, 142–147.
- 36 Z. Liu, Z. Liu, T. Cui, J. Li, J. Zhang, T. Chen, X. Wang and X. Liang, *Chem. Eng. J.*, 2014, **235**, 257–263.
- 37 S. Liu, E. Guo and L. Yin, *J. Mater. Chem.*, 2012, **22**, 5031–5041.
- 38 D. Zhao, J. Feng, Q. Huo, N. Melosh, G. Fredrickson, B. Chmelka and G. Stucky, *Science (80-. )*, 1998, **279**, 548–52.
- 39 J. Ma, L. Qiang, X. Tang and H. Li, *Catal. Letters*, 2010, **138**, 88–95.
- 40 X. Wang, F. Li, Y. Hao, S. Liu and M. Yang, *Mater. Lett.*, 2013, **99**, 38–41.
- 41 X. F. Qian, T. Kamegawa, K. Mori, H. X. Li and H. Yamashita, *J. Phys. Chem. C*, 2013, **117**, 19544–19551.
- 42 S.-Y. Chen, T. Mochizuki, Y. Abe, M. Toba and Y. Yoshimura, *Appl. Catal. B Environ.*, 2014, **148–149**, 344–356.
- 43 Y. J. Acosta-Silva, R. Nava, V. Hernández-Morales, S. A. Macías-Sánchez, M. L. Gómez-Herrera and B. Pawelec, *Appl. Catal. B Environ.*, 2011, **110**, 108–117.
- 44 K. De Witte, A. M. Busuioic, V. Meynen, M. Mertens, N. Bilba, G. Van Tendeloo, P. Cool and E. F. Vansant, *Microporous Mesoporous Mater.*, 2008, **110**, 100–110.
- 45 H. Zhang, J. Sun, D. Ma, G. Weinberg, D. S. Su and X. Bao, *J. Phys. Chem. B*, 2006, **110**, 25908–15.
- 46 L. Huang, H. Xu, Y. Li, H. Li, X. Cheng, J. Xia, Y. Xu and G. Cai, *Dalton Trans.*, 2013, **42**, 8606–16.
- 47 J.-M. Wu, *J. Phys. Chem. C*, 2008, **112**, 13192–13199.
- 48 C. Wang, C. Shao, X. Zhang and Y. Liu, *Inorg. Chem.*, 2009, **48**, 7261–7268.
- 49 Y. Duan, N. Fu, Q. Liu, Y. Fang, X. Zhou, J. Zhang and Y. Lin, *J. Phys. Chem. C*, 2012, **116**, 8888–8893.
- 50 M. Long, W. Cai, J. Cai, B. Zhou, X. Chai and Y. Wu, *J. Phys. Chem. B*, 2006, **110**, 20211–20216.
- 51 C. Xing, Y. Zhang, W. Yan and L. Guo, *Int. J. Hydrogen Energy*, 2006, **31**, 2018–2024.
- 52 P. Wardman, *J. Phys. Chem. Ref. Data*, 1989, **18**, 1637–1755.
- 53 A. Leelavathi, G. Madras and N. Ravishankar, *Phys. Chem. Chem. Phys.*, 2013, **15**, 10795–802.